

Shear processes in bulk metallic glasses

D.J. Safarik *, C.M. Cady, R.B. Schwarz *

Los Alamos National Laboratory, MST Division, Structure/Property Relations Group, Mail Stop G755, Los Alamos, NM 87545, USA

Received 30 September 2004; received in revised form 4 January 2005; accepted 14 January 2005

Available online 25 February 2005

Abstract

We investigated Newtonian and non-Newtonian flow in bulk metallic glasses by compressing cube-shape specimens that have a central hole. The hole localized deformation along well-defined shear planes, which enabled us to plastically deform the same volume of the glass specimen along differently oriented glide directions. We found that the glass has a memory of its previous plastic deformation, but this memory is largely independent of the previous glide direction. The transition from Newtonian to non-Newtonian flow is abrupt and occurs at a Deborah number, $De = \dot{\gamma} \cdot \tau$, of 0.5, where $\dot{\gamma}$ is the plastic shear strain rate and τ is the relaxation time for the annihilation of the flow defects. This value of De is consistent with that observed at the onset of flow instabilities in Newtonian liquids, which occurs at $De \approx 1$.

© 2005 Acta Materialia Inc. Published by Elsevier Ltd. All rights reserved.

Keywords: Bulk metallic glass; Viscosity; Newtonian and non-Newtonian flow; Deborah number

1. Introduction

The plastic deformation of metallic glasses is classified as either homogeneous or inhomogeneous [1]. Homogeneous flow occurs at slow imposed deformation rates and is often investigated at temperatures near and above the glass transition (T_g) [2,3]. In this regime, every element of the metallic glass contributes to the overall plastic strain. Below T_g and particularly for large imposed strain rates, plastic flow becomes inhomogeneous and tends to localize on a small number of bands that form approximately on planes of highest resolved shear stress [1,2]. The large rate of energy dissipation within a band may cause localized adiabatic heating (and even melting), and this often leads to an instability and catastrophic failure [4,5].

Without reference to any microscopic mechanism of plasticity, one can always define the viscosity, η , of the deforming solid as $\eta \propto \sigma / \dot{\epsilon}_p$, where $\dot{\epsilon}_p$ is the plastic strain

rate and σ is the stress. Experiments show that at temperatures close to T_g and for low imposed rates of deformation, the flow is Newtonian (viscosity depends only upon temperature) and the deformation is homogeneous. At high imposed rates of deformation, the flow becomes non-Newtonian and is characterized by a viscosity that depends upon both temperature and strain rate [3,6]. From a microscopic viewpoint, it is not clear whether the deformation is inhomogeneous or homogeneous during non-Newtonian flow.

Fig. 1 shows compressive stress–strain curves for $\text{Pd}_{40}\text{Ni}_{40}\text{P}_{20}$ bulk metallic glass measured at 565 K for two different imposed deformation rates, one in the Newtonian and the other in the non-Newtonian regime [6]. The lower stress–strain curve (for Newtonian flow) can be modeled as a simple Maxwell solid consisting of a spring in series with a standard dashpot [7]. The upper curve cannot be modeled by any simple combination of springs and dashpots. This curve shows a rather abrupt transition in the flow mechanism which leads to a drop in the stress. Similar upper yield point and softening phenomena are observed in other materials, including crystalline alloys [8], quasicrystals [9], inorganic

* Corresponding authors. Tel.: +1 505 667 8454; fax: +1 505 667 8021.

E-mail address: rxzs@lanl.gov (R.B. Schwarz).

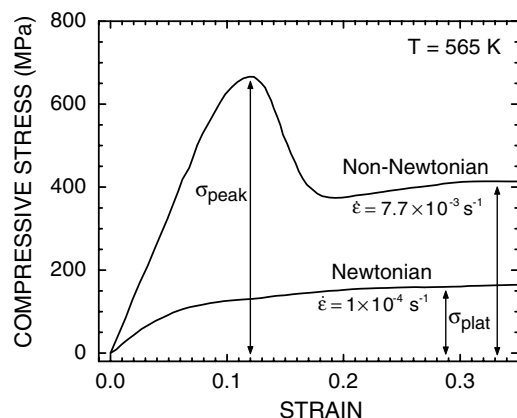


Fig. 1. Stress-strain curves for compression of Pd₄₀Ni₄₀P₂₀ bulk metallic glass at constant imposed deformation rates within the Newtonian and non-Newtonian flow regimes. σ_{peak} is the peak stress at the upper yield point and σ_{plat} is the plateau stress (Data from Nishiyama et al., Ref. [6]).

oxide glasses [10,11], and amorphous polymers [12]. These behaviors have been interpreted differently. Upper yield points in crystalline alloys are attributed to the stress-assisted generation of dislocations or to the release of aged dislocations from solute clouds. In quasicrystals, the phenomenon is believed to originate from a sudden increase in dislocation mobility at a critical applied stress [9]. Softening of metallic glasses following the peak stress (σ_{peak}) has been attributed to a transformation that takes the glass from its original structure to a dynamically different structure of lower viscosity [3,6,13–16].

Although the macroscopic characteristics of metallic glass plasticity have been identified and classified [1], the microscopic features of plasticity are still debated. Attaining a microscopic understanding of plasticity in glassy metals has proven difficult, largely because the lack of long-range order in the glass precludes imaging of the atoms participating in the deformation, something that is easily done in crystals with electron microscopy.

Similarities in the mechanical behavior of all metallic glasses suggest a common mechanism of plastic flow. In crystals and quasicrystals, the common mechanism of plastic deformation is the non-conservative generation and motion of dislocations [17]. Dislocation glide processes have also been suggested as the origin of plasticity in amorphous alloys [18,19], but this mechanism has not been supported by observation nor by computer modeling. At low stresses, glass plasticity has been attributed to uncorrelated, thermally activated atomic jumps into “holes” or regions of excess “free volume” in the structure [20]. Spaepen [1] developed this concept quantitatively as it applies to glasses. The model assumes that, as in liquids, flow occurs by means of atomic jumps that are biased in the direction of a shear-

ing force. Whereas in liquid-flow theories a jump can occur only when random density fluctuations create an adjacent hole large enough to accommodate an atom [21], Spaepen proposed that at high stresses an atom can be forced to squeeze into a hole whose volume is smaller than that of the jumping atom. Provided the hole left behind does not collapse, this process may result in a strain-induced net increase of free volume, which makes future atomic jumps easier and thus decreases the viscosity. In this theory, creation of free volume continuously competes with diffusive relaxation processes that annihilate free volume and densify the glass.

Free-volume models of plasticity necessarily lead to two predictions: (1) free volume should increase during plastic deformation (eventually attaining a plateau value); (2) hydrostatic pressure should influence flow and fracture. This first prediction has been confirmed through density [22] and heat capacity [23,24] measurements on metallic glasses deformed in the non-Newtonian regime. The preferential etching of shear bands formed during inhomogeneous flow at low temperatures may also support this prediction [25]. The second prediction has not been borne out experimentally, at least not for the inhomogeneous deformation regime [26,27]. Although the free-volume model correctly predicts that flow should be Newtonian at low stresses, at higher stresses the viscosity is observed to decrease more rapidly with stress than predicted by the free-volume model [28]. This deviation suggests that the shear events participating in Newtonian and non-Newtonian flow are different. Because shear events cannot be observed directly in amorphous materials, researchers have tried to elucidate their nature through physical modeling and computer simulations.

The bubble raft experiments (physical simulations) of Argon and Kuo [29] revealed two types of localized shear events, each involving a small number of “atoms”: (1) diffuse rotational shear events, consisting of cooperative bubble motions in equiaxed regions about 5 bubbles in diameter; (2) sharp shear translations between two adjacent, close-packed bubble rows, about 4–6 bubbles in length. The former shear events occurred preferentially at sites of reduced bubble density (excess “free area”), whereas the latter tended to take place in close-packed regions having little excess free area. Both types of shear events generated, at least temporarily, excess free area. Argon and Shi [30,31] later used these findings to formulate quantitative models of plastic deformation in metallic glasses.

Further insight into microscopic mechanisms of metallic glass plasticity has been attained through computer modeling. The three-dimensional computer simulations of Srolovitz et al. [32] on a monatomic metallic glass (2067 atoms, periodic boundary conditions) being deformed by shear at zero pressure and zero tempera-

ture revealed an upper yield point in the stress–strain curve, followed by softening, similar to that shown in Fig. 1. Three types of structural “defects”, designated p , n , and τ , were defined as regions of the glass where the atomic-level non-deviatoric and deviatoric stresses exceeded arbitrarily defined threshold levels. p -Type and n -type defects were defined by regions of large positive and negative internal pressures, and hence positive and negative local fluctuations from the mean density. τ -Defects, on the other hand, were defined by areas of large deviatoric stresses. Two important findings emerged from this work. First, shear deformations occurred mainly in regions of concentrated deviatoric stresses (τ -defects) rather than regions with an excess (n -defects) or deficiency (p -defects) of free volume. Shear events therefore neither required nor made use of free-volume. Second, the τ -defects disappeared when the applied stress was removed, but reappeared at the same sites when the glass was sheared again in the same direction. Reloading in a different orientation did not reactivate the same τ defects.

More recent computer simulations [13–15] performed for a constant sample volume have all reproduced the upper yield point in the stress–strain curve, implying that the net creation of free volume is not necessary for the appearance of the yield point. None of these simulations gives an indication of the structure of the shear event (number of atoms and their motion, etc.). Further simulations on the structure of supercooled liquids [33,34] and metallic glasses [35] have revealed cooperative, string-like thermal motions. Within such strings, atoms have a much greater mobility than in the surrounding matrix and tend to move in the same direction as adjacent mobile atoms. Similar cooperative string-like motion has been observed in two- and three-dimensional colloidal suspensions near the glass transition [36,37]. It is not known whether these strings actually exist in metallic glasses, and if they do what role they might play in plasticity.

The interstitialcy theory of Granato and co-workers [38,39] is explicit about the nature of the defects responsible for plasticity in glasses. In this theory, liquids and glasses are hypothesized to be crystals containing on the order of 10% interstitial defects in a dumbbell configuration. A unique feature of interstitial defects is their large contribution to the entropy and shear compliance of a material. As a result, even small increases in the concentration of interstitials (caused by shearing) can significantly reduce the shear modulus and viscosity of the glass.

Indirect information about the nature of plasticity shear events in metallic glasses has been obtained by measuring changes in density, mechanical properties, and structure of the glass as a function of plastic deformation and annealing. Harms et al. [22] showed that deformation of bulk $\text{Pd}_{40}\text{Ni}_{10}\text{Cu}_{30}\text{P}_{20}$ glass in the non-

Newtonian flow regime causes a decrease in both the glass density and shear modulus, but leaves the bulk modulus effectively unchanged. They found a relative change in the shear modulus with respect to the density of $d(\ln G)/d(\ln \rho) = 25$. This ratio suggests that if non-Newtonian deformation does make use of distinct plasticity defects, they have large shear compliance.

Using energy-dispersive X-ray diffraction, Suzuki et al. [40] showed that following creep deformation of $\text{Fe}_{40}\text{Ni}_{40}\text{Mo}_3\text{Si}_{12}\text{B}_5$ glass, the radial distribution function in the direction parallel to the applied load is different than for the direction perpendicular to the load. Furthermore, mechanical torsion tests involving the alternating twisting of a metallic glass have revealed behavior similar to the Baushinger effect in crystals [41]. These last two studies suggest that metallic glasses may have a directional memory of previous plastic deformation.

The computer simulations and indirect experimental evidence mentioned above provide an incomplete picture of plasticity in metallic glasses. Among the important unresolved questions are: (1) What is the structure of the “shear events” at the atomistic level and how do they contribute to flow? (2) Are the shear events operating during Newtonian and non-Newtonian flow the same, differing only in their number and possibly their spatial distribution? (3) Does the transition from Newtonian to non-Newtonian flow (as seen, for example, on plotting $\eta = \sigma/3\dot{\epsilon}_p$ vs. $\dot{\epsilon}_p$ [3,6] measured in compression tests) correlate with a transition from homogeneous to inhomogeneous flow? The present work addresses some of these questions. Specifically, we investigate whether the shear events in non-Newtonian flow have directional memory. We address this question by performing multiple compression tests on cube-shaped specimens with central holes, plastically deforming each sample in at least two of its three possible loading orientations. In this way, we probe whether non-Newtonian plastic flow during the initial deformation results in loading-direction-dependent deformation in subsequent compression tests that activate other slip directions. Our work reveals that deformation does depend upon the flow history but this memory does not show any directionality. Furthermore, we find that the transition from Newtonian to non-Newtonian flow occurs at a Deborah number, $De = \dot{\gamma} \cdot \tau$, of ≈ 0.5 , where $\dot{\gamma}$ is the shear strain rate and τ is the relaxation time constant for the annihilation of the flow defects. This value of De corresponds well with the critical value of $De \approx 1$ observed at the Newtonian to non-Newtonian transition in liquids.

2. Experimental

Glassy $\text{Pd}_{40}\text{Ni}_{40}\text{P}_{20}$ rods were synthesized from elemental Pd powder, Ni powder, and phosphorous

chunks, as reported previously [22]. Compression specimens were prepared by electro-discharge machining. After machining, all test specimens were annealed for 18 h at 553 K ($T_g = 578$ K, $T_x = 660$ K) in a purified Ar atmosphere (<1 ppm oxygen) to structurally relax the alloy. At the conclusion of the annealing period, each sample was rapidly cooled to preserve in the glass the amorphous microstructure and short-range order characteristic of the annealing temperature. No trace of crystallinity could be detected at this stage with either X-ray diffraction or differential scanning calorimetry (DSC). The latter technique was used to measure the enthalpy of crystallization, which decreases rapidly with increased ordering in the glass.

Compression tests were performed on cube-shaped samples shown schematically in Fig. 2. Each sample measured $5.1 \times 5.1 \times 5.1$ mm³ and had a 1.7 mm diameter hole parallel to the x -axis. Fig. 3 shows the results of an elastic finite element calculation for compression parallel to the z -axis. The curves correspond to contours of constant von Mises shear stresses, with the numbers indicating the relative values of the stress. Because of the elastic distortions associated with the hole, the shear stresses are highest along four bands that are aligned parallel to the hole and extend outward from it at $\approx 45^\circ$. The arrows in Fig. 3 indicate the relative shear directions within these bands. Compression along the y -direction creates an analogous stress distribution to that shown in Fig. 3, except that the shear directions are reversed. Notice further that for compression along the z -direction the maximum shear stress is located at the ends of the arrow labeled C, whereas for compression along the y -direction, the maximum shear stress is located at the ends of the arrow labeled D. The situation is quite different for compression along the x -direction. Here, the planes of highest shear stress are also oriented at 45° to the compression direction, but in this case the

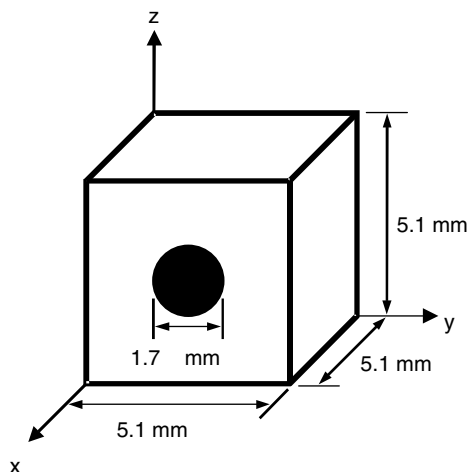


Fig. 2. Schematic of compression test specimens.

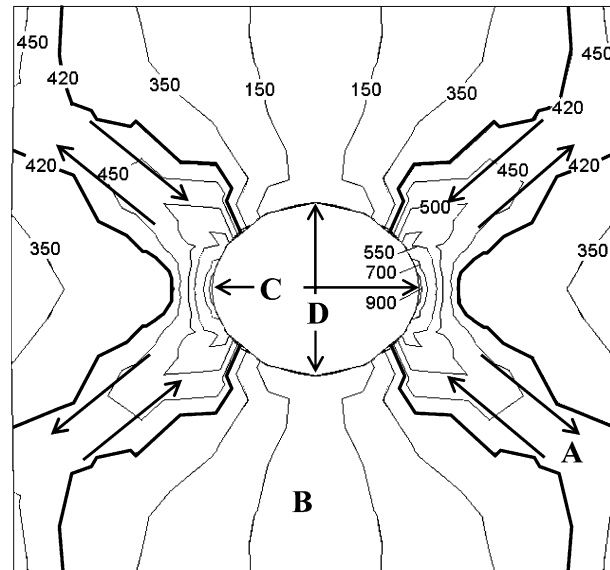


Fig. 3. Contours of constant von Mises shear stress for a cube-shaped specimen compressed parallel to the z axis. The numbers on the contours indicate the relative values of the stress. The heavy curves delineate bands of maximum shear stresses and the arrows indicate the relative direction of shear within the bands. Note that the specimen is elastically deformed, resulting in distortion of the circular hole.

hole (now parallel to the loading direction) plays no role and the stresses are delocalized throughout the specimen.

We performed both constant-deformation-rate (referred to as constant-strain-rate) and creep compression tests at a temperature of 553 K, the same temperature used in the 18-h anneal. Constant-strain-rate experiments were conducted on either a screw-driven testing machine (Applied Test Systems model 1120, Butler, PA) or a hydraulically driven test machine (MTS model 880, Eden Prairie, MN) at an initial strain rate of $\dot{\epsilon} = 2 \times 10^{-4}$ s⁻¹. Creep experiments were performed on the same hydraulically driven test machine using a constant applied load. Normally, 2–3 min elapsed between first placing the sample on the pre-heated platens of the deformation machine and the start of the compression test. Following deformation, the samples were rapidly unloaded, removed from the platens, and quenched in water to preserve the amorphous microstructure and short-range order present at the end of each compression test. Approximately 10 s elapsed between the conclusion of the compression tests and the water quench.

3. Results

3.1. Localization of the deformation in narrow bands

The finite element calculations [42] in Fig. 3 predict that for compression along the z and y directions, plastic

flow should localize along the four diagonal shear bands. We verified this localization by deforming a sample, removing aliquots from various regions of the deformed sample, and measuring their heat capacity near T_g with DSC. The two curves in Fig. 4 show the heat flow for ~ 20 mg aliquots cut from regions A and B in Fig. 3, respectively. The peak in the heat flow is clearly smaller for the aliquot removed from region A, which was subjected to larger shear stresses. This correlation between plastic deformation and peak height has been reported earlier [24,43]. The excess enthalpy release is a kinetic effect due to the finite heating rate used during the DSC experiments. This peak is larger in curve B (minimally deformed alloy) than in curve A (heavily deformed alloy) because diffusion is slower in the minimally deformed material. These calorimetric results are consistent with our visual observations of flow localization.

Localization of the flow into narrow bands during compression along the z and y axes both confines the region of deformation and defines the shear direction. This is analogous to planar Couette flow, where a fluid confined between two parallel plates is sheared by imposing a velocity gradient between the plates [44]. By contrast, for compression along the x -axis the stress is delocalized. As a result, the volume that deforms as well as the shear direction are poorly defined; shearing occurs along a large number of intersecting planes of maximum resolved shear stress.

3.2. Kinetics of defect annihilation

Throughout this paper, compressive stress is given by $\sigma = F/A_0$, where F is the applied load and A_0 is the initial cross-section at the center of the sample, which does not include the area of the hole. We use engineering stress,

rather than true stress, because for compression parallel to the y and z directions (Fig. 2) the deformation is localized in four shear bands whose area remains approximately constant during the tests. Engineering stress is also used for compressions in the x -direction. Here, the sample cross-section again does not include the area of the hole.

Fig. 5 is a plot of compressive stress vs. strain for three different specimens, each loaded parallel to the z -axis at 553 K and $\dot{\epsilon} = 2 \times 10^{-4} \text{ s}^{-1}$. After attaining a peak value, the stress asymptotically approaches a plateau value. Assuming that the softening after the peak stress is due to a rapid increase in the density of flow defects, then the plateau should represent a balance between the rates of defect generation and annihilation. The purpose of the tests in Fig. 5 was to measure the kinetics of defect annihilation. To accomplish this, for two of the three specimens the deformation was interrupted and the samples were rapidly unloaded to zero applied stress. The samples were then annealed at 553 K for specified times and then deformed again at the same strain rate. The quantity of interest during the recompression was the amplitude of the stress overshoot, $\Delta\sigma$, as a function of annealing time.

Fig. 6 shows $\Delta\sigma$ as function of zero-load annealing time at 553 K. Here, $\Delta\sigma$ is normalized by the amplitude of the initial stress overshoot, $\Delta\sigma_0$, as indicated in the inset to the figure. The $\Delta\sigma/\Delta\sigma_0$ vs. annealing time data in Fig. 6 are well fit by a simple exponential response function

$$\frac{\Delta\sigma}{\Delta\sigma_0} = 1 - \exp\left(-\frac{t}{\tau}\right) \quad (1)$$

with τ ($T = 553 \text{ K}$) = 1260 s.

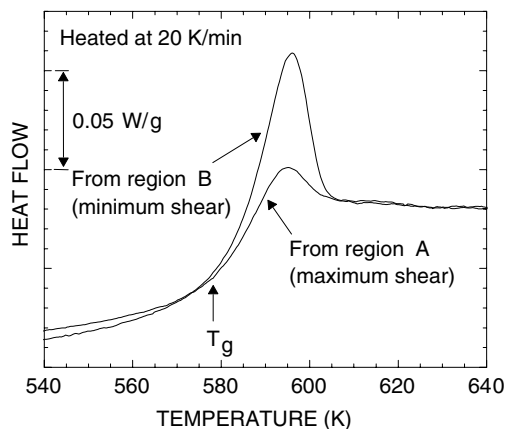


Fig. 4. Heat flow versus temperature near T_g following plastic deformation of cube-shaped specimens of amorphous $\text{Pd}_{40}\text{Ni}_{40}\text{P}_{20}$. One curve is for an aliquot removed from a band of maximum shear stress (region A in Fig. 3), and the other is for an aliquot taken from a region of minimum shear stress (region B in Fig. 3).

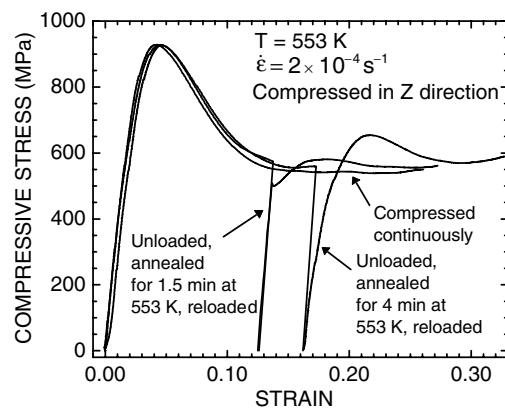


Fig. 5. Stress-strain curves for constant-strain-rate compression parallel to the z axis for three different specimens. One sample was deformed continuously, while deformation of the other two was interrupted by a zero-load anneal at 553 K. The strain rate in these experiments was $2 \times 10^{-4} \text{ s}^{-1}$, except for *reloading* of the specimen annealed for 1.5 minutes, where $\dot{\epsilon}$ was initially $8 \times 10^{-4} \text{ s}^{-1}$ but was reduced to $2 \times 10^{-4} \text{ s}^{-1}$ just below the plateau stress.

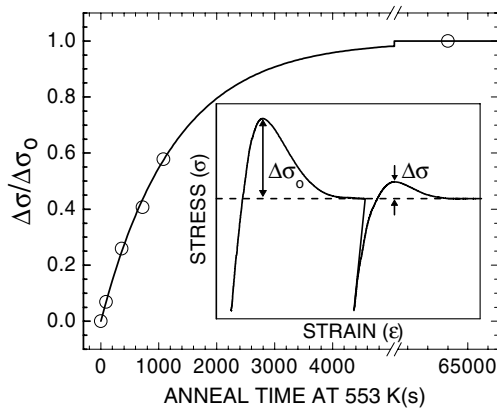


Fig. 6. Normalized stress overshoot, $\Delta\sigma/\Delta\sigma_0$, as a function of the intermediate annealing time at 553 K.

3.3. Constant strain rate tests at 553 K

Fig. 7 shows compression stress–strain curves for the same specimen deformed first in the z and then the y -direction. The insets of Fig. 7 highlight the bands of maximum shear stress predicted by the elastic finite-element calculations [42]. This will be discussed further in Section 4. During the first loading (z -direction), the cube was compressed to 16% strain at $\dot{\epsilon} = 2 \times 10^{-4} \text{ s}^{-1}$ and then was quickly unloaded and quenched in water. The two faces normal to the y -axis (see Fig. 2) were polished flat and parallel, and the specimen was then compressed in the y -direction. Initially, the strain rate for the second compression was $\dot{\epsilon} = 8 \times 10^{-4} \text{ s}^{-1}$, but was reduced to $2 \times 10^{-4} \text{ s}^{-1}$ as the plateau stress was approached. Both the first and second compressions show a stress overshoot, but the overshoot is significantly smaller in the second compression than in the first.

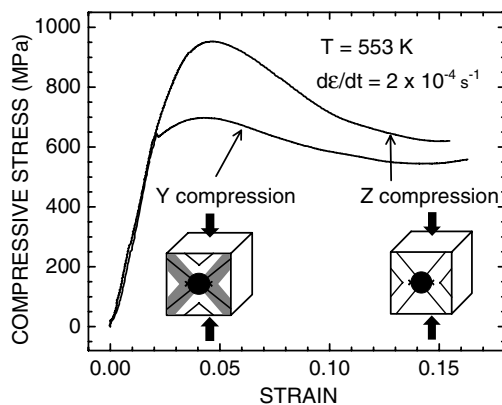


Fig. 7. Compressive stress–strain curves for a cube-shaped specimen deformed first along the z axis and then along the y axis. The strain rate for the z compression was of $2 \times 10^{-4} \text{ s}^{-1}$. For deformation in the y direction, the strain rate was initially $8 \times 10^{-4} \text{ s}^{-1}$, but at $\sim 600 \text{ MPa}$ was reduced to $\dot{\epsilon} = 2 \times 10^{-4} \text{ s}^{-1}$. The inset diagrams highlight the points of maximum shear stress (left and right edges of the hole) and the shear bands. Shear bands for the first compression are light and those for the second are dark.

Fig. 8 shows compression stress–strain curves for a specimen deformed first in the z -direction and then in the x -direction, both at $\dot{\epsilon} = 2 \times 10^{-4} \text{ s}^{-1}$. Both compression tests show a stress overshoot, with the overshoot again significantly smaller in the second test than in the first.

Fig. 9 shows compression stress–strain curves for a specimen deformed first in the x -direction and then in the z -direction, both at a strain rate of $2 \times 10^{-4} \text{ s}^{-1}$. A stress overshoot is again observed in the second compression test, but now it is even smaller than that seen in the second compressions in Figs. 7 and 8.

For each deformation shown in Figs. 7–9, the maximum strain was $\approx 16\%$. All of these tests were repeated with smaller total strains of about 5%, which is just past the peak stress in the loading curve. The results were qualitatively the same as those shown in Figs. 7–9 and thus will not be discussed further.

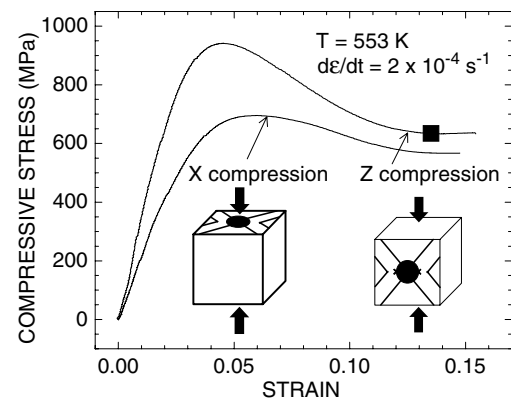


Fig. 8. Stress–strain curves for compression of the same sample first in the z direction and then in the x direction. Both tests were performed at $\dot{\epsilon} = 2 \times 10^{-4} \text{ s}^{-1}$. Shear bands formed in the first compression are illustrated in the inset diagram; the hole does not cause shear stress localization for the second compression. Attainment of the plateau stress during compression in the z direction is indicated by the solid square. This symbol corresponds to the solid square in Figs. 11 and 12.

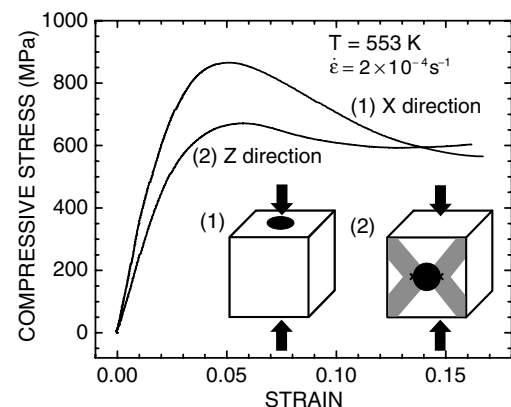


Fig. 9. Compressive stress–strain curves for deformation of the same specimen along the x axis and then along the z axis. Both tests were performed at $\dot{\epsilon} = 2 \times 10^{-4} \text{ s}^{-1}$. Shear bands formed during z compression are shaded in the inset diagram.

3.4. Creep tests at 553 K

Fig. 10 shows plastic strain vs. time curves for creep compression tests at 553 K. In each test the load was constant and equivalent to an initial normal stress of 685 MPa. Note that this stress is less than the peak stress in Fig. 5, but greater than the plateau stress. For the first creep compression in the z -direction, there is an initial period of slow deformation that lasts for about 300 s. The creep rate then accelerates and asymptotically approaches a new, faster rate. For the temperature and stress shown in Fig. 10, the “incubation” time required to establish the fast creep rate, as determined by extrapolation of the strain vs. time curve to the abscissa, is 450 s.

When the cube-shaped specimen is rapidly unloaded, rotated, and reloaded in the x -direction, the initial period of slow creep is absent (curve (2) in Fig. 10). Rather, the fast creep rate is established almost immediately, requiring an incubation time of only 80 s.

3.5. Viscosity of the deforming alloy

Fig. 11 is a plot of viscosity vs. shear stress for samples compressed along the z -direction at 553 K. As we have seen, the stress concentration due to the hole forces the deformation to take place along four shear bands, rather than uniformly throughout the whole specimen. This strain localization is somewhat analogous to Couette flow experiments usually performed on liquids and alluded to earlier. The advantage of localizing the deformation into narrow bands is that the flow field is better defined and the viscosity follows simply from the ratio $\eta = \sigma_{\text{shear}} / \dot{\gamma}$, where $\dot{\gamma}$ is the plastic shear strain rate and σ_{shear} is the shear stress. Since the bands were oriented at $\approx 45^\circ$ to the compressive load, $\sigma_{\text{shear}} = \sigma/2$. $\dot{\gamma}$ was com-

puted by first determining the plastic normal strain rate. Then, using the shear band orientation and estimated band thickness of 0.5 mm, we converted the normal strain rate to a shear strain rate. All plastic strain was assumed to occur in the bands, which agrees with the observed macroscopic deformation of the samples. For the constant-strain-rate test (open squares in Fig. 11), $\dot{\gamma}$ was calculated by subtracting the elastic strain from the total strain and then differentiating this quantity with respect to time. The elastic strain was calculated from the applied normal stress and the estimated Young's modulus of the alloy. For this test the viscosity is initially constant (as expected for Newtonian flow) but then decreases rapidly once the shear stress exceeds about 350 MPa. Even after reaching the peak shear stress of about 500 MPa, the viscosity continues to decrease. For the two creep tests at constant stress (open circles and open triangles), the viscosity decreases with increasing strain. Note that for a given value of the applied stress, there can be different values of viscosity depending upon the deformation history.

The solid symbols (square, circle, and triangle) in Fig. 11 denote the values of viscosity measured when the sample had attained the plateau stress (solid square in Fig. 8) and the fast and steady creep rate (solid circle in Fig. 10). The dashed line in Fig. 11 joining the solid symbols gives the approximate viscosity that is expected when the deformation has achieved a steady state, either in constant-strain-rate tests or in creep tests. An extrapolation of this line indicates that to maintain the deformation within the Newtonian regime at 553 K, one must keep the applied shear stress below ≈ 190 MPa (normal stress below ≈ 380 MPa). This value of stress is in good agreement with the observed onset of non-Newtonian flow in the constant deformation rate test (open squares), given the uncertainty in judging the break point in the η vs. σ_{shear} data. Similar behavior was

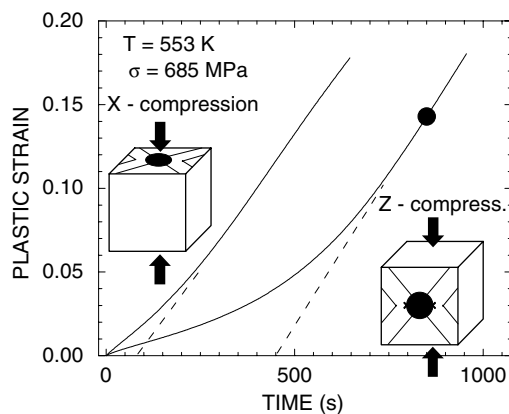


Fig. 10. Plastic strain versus time for creep deformation of the same sample in the z direction and then in the x direction. The applied normal stress for both compressions was 685 MPa. Attainment of steady-state at the fast creep rate for compression in the z direction is indicated by the solid circle. This symbol corresponds to the solid circle in Figs. 11 and 12.

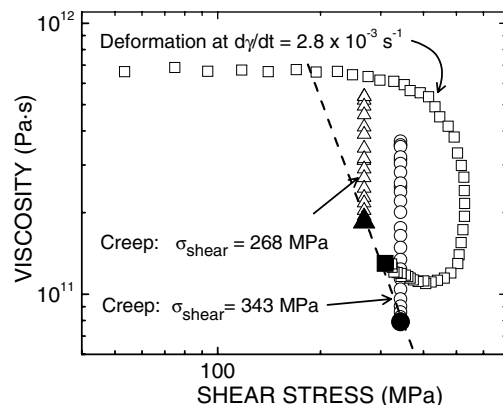


Fig. 11. Viscosity versus shear stress (in the shear bands) for compression of cube-shaped specimens along the z axis at 553 K. The solid symbols denote the value of the viscosity at steady-state for the three experiments.

observed by Chen and co-workers [6], who plotted data for steady-state flow of Pd₄₀Ni₄₀P₂₀ glass at the plateau stress.

In Fig. 12, the viscosity data from Fig. 11 are plotted vs. plastic shear strain rate. The main difference with Fig. 11 is that all the data now fit nicely into two clearly identified regimes, separated by a critical plastic shear strain rate, $\dot{\gamma}_c$, of about $3.7 \times 10^{-4} \text{ s}^{-1}$. The flow is Newtonian below $\dot{\gamma}_c$ but changes rather abruptly to non-Newtonian for $\dot{\gamma} > \dot{\gamma}_c$.

In the non-Newtonian regime, the viscosity depends on strain rate, stress, and deformation history. Because σ_{shear} is constant during a creep test, plots of $\ln(\eta)$ vs. $\ln(\dot{\gamma})$ are straight lines with slope -1 . Since σ_{shear} varies during the constant-deformation-rate test, $\ln(\eta)$ vs. $\ln(\dot{\gamma})$ is curved, most notably at the “hook” at high strain rates. The solid symbols (square, circle, and triangle) in Fig. 12 indicate the values of viscosity when the sample had reached the plateau stress (solid square in Fig. 8) or the fast creep rate (solid circle in Fig. 10). The dashed line in Fig. 12 joining the solid symbols gives the approximate viscosity that is expected when deformation has achieved steady state, either in constant-deformation-rate or creep tests. The slope of this line is $d\ln(\eta)/d\ln(\dot{\gamma}) \approx -0.8$. Extrapolation of the line indicates that to maintain deformation in the Newtonian regime at 553 K, the imposed shear strain rate must be kept below $2.8 \times 10^{-4} \text{ s}^{-1}$. This is in good correspondence with the value of $\dot{\gamma}_c$ considering the uncertainty in judging the location of the break point in the η vs. $\dot{\gamma}$ data (open squares). Note in Fig. 12 that the plastic shear strain rate can exceed the imposed rate of $2.8 \times 10^{-3} \text{ s}^{-1}$. This occurs when the applied stress drops and some of the elastic energy stored in the test machine is dissipated through deformation of the sample.

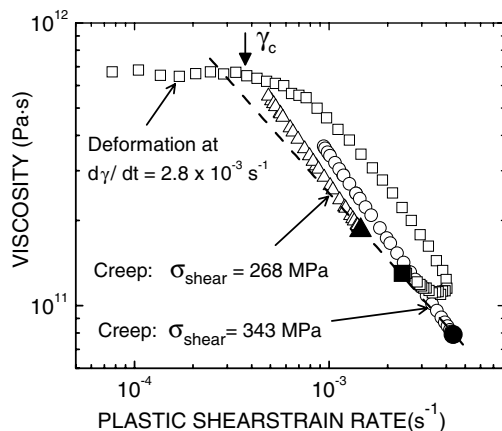


Fig. 12. Viscosity versus plastic shear strain rate (in the shear bands) for compression of cube-shaped specimens along the z axis at 553 K. $\dot{\gamma}_c$ is the critical plastic shear strain rate for the transition from Newtonian to non-Newtonian flow. The solid symbols denote the values of the viscosity at steady-state flow for the three experiments.

4. Discussion

4.1. Memory and directionality of the shear events

The experiments in Fig. 5 test the memory of the plasticity shear events (or “defects”) active in the non-Newtonian flow regime, and in doing so, help us elucidate the structure of these defects. If the sample is unloaded and then reloaded after a short anneal at 553 K, the deformation continues at nearly the same stress as before unloading. As the zero-load anneal time increases, the ensuing stress–strain curve shows a stress overshoot. This indicates that some of the shear defects generated during the first deformation have been annealed out or are unable to contribute to plastic flow during the second compression. The increase in the overshoot amplitude with anneal time (Fig. 6) follows first-order kinetics, with a recovery time constant of 1260 s at 553 K.

The free-volume model [1] assumes that deformation occurs through a superposition of stochastic single atomic jumps, and that each jump creates excess free volume. In the framework of this model, the recovery time of 1260 s would be attributed to the diffusional annihilation of free volume. This would agree with the small densification ($\approx 0.1\%$) observed upon annealing a glass that has been plastically deformed in the non-Newtonian flow regime [22]. However, the plastic deformation also causes a decrease in the shear modulus of 4% (about 25 times larger than the change in free volume!). It was argued in [22] that this large modulus change cannot be attributed to isolated vacancy-type defects in the glass. Thus, although the free-volume model may explain creep in the Newtonian regime, it cannot reproduce some of the observations for flow in the non-Newtonian regime.

In the non-Newtonian deformation regime, the flow is most likely the result of collective atomic motions. This would lead to a rapid increase in the strain per thermally activated event (relative to the events in the Newtonian regime), with little or no increase in flow stress. The viscosity would therefore decrease quickly with increasing imposed stress or imposed strain rate, as is seen in Figs. 11 and 12. Also, the presence of shear defects (regions of reduced short-range order and high shear compliance) may explain the large decrease in shear modulus following deformation. Therefore, the relaxation time constant of 1260 s (Fig. 6) may reflect the annihilation of these extended defects, which might occur concurrently with the annihilation of free volume, as suggested in [22].

Although the results in Figs. 5 and 6 indicate that the shear defects have memory, they do not tell us whether the defects are directional. The tests described in Figs. 7–9 were designed to address this question. In the two compression tests shown in Fig. 7, the sample was sheared in succession along the same glide planes, but

between tests the shear direction was reversed. If the shear events have directionality, and if few of them are annihilated during the short time taken to unload and reload the sample, then the stress–strain curve for the second compression (y -direction) should have shown no stress overshoot. This second curve, however, does show an overshoot. Two effects may have contributed to this overshoot: (1) annihilation of the plasticity agents; (2) non-coincidence of the deformation regions. These two effects will now be discussed.

To change the direction of compression, the sample had to be unloaded and reloaded, and this resulted in an unintended anneal of ≈ 3 min. According to Fig. 6, this anneal time should cause a recovery in the overshoot stress of $\approx 13\%$, which is about one-fourth to one-third of the observed value of $\Delta\sigma/\Delta\sigma_0$. Regarding the second effect, note that the shear bands for compression in the z and in the y directions do not overlap completely, as shown in the inset of Fig. 7. Furthermore, as seen in Fig. 3, the regions of *maximum* shear stress for compression in the z -direction are located at the ends of arrow C, whereas for the second compression (along the y -axis) they are located at the ends of arrow D. These points do not overlap. This means that in the second deformation the shear bands had to initiate from a partially “virgin” region of the glass.

For the two compression tests in Fig. 8, plastic deformation was forced to occur on differently oriented glide planes and in different glide directions. If this change would have required the generation of completely new non-Newtonian plasticity agents, then the second compression (along the x -axis) should have a stress overshoot of the same magnitude as in the first deformation. The fact that the second stress overshoot is $\approx 50\%$ smaller than the first one suggests that a fraction of the defects generated during the first compression (z -direction) were able to contribute to the ensuing deformation along the x -axis. This conclusion is also supported by the smaller initial slope of the stress–strain curve for the second loading, which indicates that significant viscous flow is occurring at stresses far below the yield point. The overshoot during the second deformation arises from the generation of defects in regions of the specimen that were not deformed during the first compression.

In summary, the results in Figs. 7 and 8 suggest that the non-Newtonian plasticity agents may not have directional memory or, if they do have directional memory, they lose it in a very short time, shorter than 3 min at 553 K. The results in Fig. 9 point to the same conclusions. Similar to the tests in Fig. 8, in the two experiments in Fig. 9 the glass was forced to shear along glide planes oriented 45° apart. As observed previously, the overshoot in the second stress–strain curve is significantly smaller than that in the first test, implying the plasticity defects formed in the first deformation partic-

ipated in the second. The creep tests in Fig. 10 further support the conclusion of apparent non-directional memory of the shear events. If the defects had directional memory, then changing the loading direction from z to x would have required a long incubation time for the formation of new shear defects and would have resulted in a similarly long delay time for the establishment of the fast creep rate. This was clearly not the case, suggesting that the plasticity agents generated during the first creep deformation were able to change glide plane orientation and glide direction and immediately participate in the second creep deformation.

4.2. Transition from Newtonian to non-Newtonian flow

The data in Figs. 11 and 12 indicate that for a given temperature, the strain rate in the non-Newtonian flow regime is a function of stress and deformation history. In this regime, deformation history plays a fundamental role because the dynamic structure is determined through a balance of defect creation and annihilation. During the creep tests at constant stresses of 268 and 343 MPa, the viscosity decreased by almost an order of magnitude. This decrease corresponds to the creation of additional agents of plasticity. The dependence of viscosity on shear stress at steady-state flow follows the dashed line in Fig. 11, which has a slope of $d\ln(\eta)/d\ln(\sigma_{\text{shear}}) \approx -3.4$. There is no indication in the present data of a limiting stress at which the viscosity decreases at an infinite rate, as suggested by Nishiyama et al. [6].

In Fig. 12, the transition from Newtonian to non-Newtonian viscosity is rather abrupt. The break in the curve at $\dot{\gamma}_c$ corresponds to a fast increase in strain rate with little change in stress. The sharpness of the transition suggests a change in the deformation mechanism brought about by the activation of a different class of plasticity agents.

Several criteria have been used to characterize flow instabilities in Newtonian liquids [45]. The Deborah number, $De = \dot{\gamma} \cdot \tau$, is often used to evaluate the stability of isothermal Newtonian flow. A transition from stable Newtonian flow to non-Newtonian flow typically occurs at $De \approx 1$. When $De \ll 1$, the liquid has plenty of time to recover its structure following a thermally activated deformation event, so that successive events have no memory and can be treated as stochastic. Single-atom jump models based upon transition-state theory should be fully applicable in this regime. When $De > 1$, on the other hand, deformation-induced structural changes are introduced more quickly than they can be relaxed. In this case shear events are no longer stochastic but depend on the previous shear event history. From the τ value determined in Fig. 6 and the $\dot{\gamma}_c$ value in Fig. 12, we calculate that for the constant-strain-rate test the transition from Newtonian to non-Newtonian flow occurs at $De = 0.5$. This correspondence to the critical Deborah

number of $De \approx 1$ is good in view of the uncertainty in determination of $\dot{\gamma}$ (we simply estimated the shear band width to be 0.5 mm based upon visual observations).

5. Conclusions

The stress–strain relationship during non-Newtonian flow depends strongly on the deformation history of the glass. This “memory” of previous plastic flow persists even after removal of the applied stress but is lost upon annealing. Loss of the memory follows first order kinetics with a time constant of 1260 s at 553 K. The memory of previous plastic deformation is largely non-directional, suggesting that the flow agents are either not directionally oriented or quickly lose their directional orientation after unloading.

The transition from Newtonian flow to non-Newtonian flow is abrupt. For $\text{Pd}_{40}\text{Ni}_{40}\text{P}_{20}$ glass at 553 K, the transition occurs at a critical shear stress of about 190 MPa and a critical shear strain rate of $3.7 \times 10^{-4} \text{ s}^{-1}$. The Deborah number at the transition is $De = 0.5$, which is close to the $De \approx 1$ value at which the onset of flow instabilities is observed in liquids. The sharpness of the transition, combined with the strong stress sensitivity of the viscosity in the non-Newtonian regime, suggests that the agents of plasticity in the Newtonian and non-Newtonian regimes are different.

Acknowledgements

The authors thank Dr. Greg Swadener, Los Alamos National Laboratory, for performing the finite-element calculations. This research was funded by the Los Alamos National Laboratory Directed Research and Development (LDRD) Program.

References

- [1] Spaepen F. *Acta Metall* 1977;25:407.
- [2] Schwarz RB. In: Westbrook JH, Fleischer RL, editors. *Intermetallic compounds*. New York: Wiley; 2002. [chapter 32].
- [3] Kato H, Kawamura Y, Inoue A, Chen HS. *Appl Phys Lett* 1988;73:3665.
- [4] Leamy HR, Chen HS, Wang TT. *Metall Trans* 1972;3:699.
- [5] Spaepen F, Turnbull D. *Scripta Metall* 1974;8:563.
- [6] Nishiyama N, Kato H, Saida J, Inoue A, Chen HS. *Jpn J Appl Phys* 2002;41:741.
- [7] Nowick AS, Berry BS. *Anelastic relaxations in crystalline solids*. New York: Academic Press; 1972.
- [8] Tabor D. *Gases, liquids, and solids*. Cambridge: Cambridge University Press; 1979.
- [9] Texier M, Bonneville J, Proult A, Rabier J, Baluc N, Guyot P. *Scripta Metall* 2003;49:41.
- [10] Brückner R. In: Cahn RW, Haasen P, Kramer EJ, editors. *Materials science and technology: a comprehensive treatment. Glasses and amorphous materials*, vol. 9. New York: VCH; 1991. p. 704.
- [11] Simmons JH, Mohr RK, Montrose CJ. *J Appl Phys* 1982;53:4075.
- [12] Narisawa I, Ishikawa M, Ogawa H. *J Polym Sci Phys Ed* 1978;16:1459.
- [13] Heyes DM, Kim JJ, Montrose CJ, Litovitz TA. *J Chem Phys* 1980;73:3987.
- [14] Utz M, Debenedetti PG, Stillinger FH. *Phys Rev Lett* 2000;84:1471.
- [15] Brinkmann K, Teichler H. *Phys Rev B* 2002;66:184205.
- [16] Chen HS, Kato H, Inoue A, Saida J, Nishiyama N. *Appl Phys Lett* 2001;79:60.
- [17] Wollgarten M, Beyss M, Urban K, Liebertz H, Köster U. *Phys Rev Lett* 1993;71:549.
- [18] Gilman JJ. *J Appl Phys* 1973;44:675.
- [19] Ashby MF, Logan J. *Scripta Metall* 1973;7:513.
- [20] Turnbull D, Cohen MH. *J Phys Chem* 1970;52:3088.
- [21] Glasstone S, Laidler KJ, Eyring H. *The theory of rate processes*. New York: McGraw-Hill; 1941. [chapter 9].
- [22] Harms U, Jin O, Schwarz RB. *J Non-Cryst Solid* 2003;317:200.
- [23] Van Den Beukel A, Sietsma J. *Acta Metall Mater* 1990;38:383.
- [24] de Hey P, Sietsma J, van den Beukel A. *Mater Sci Eng* 1997;A226–228:336.
- [25] Pampillo CA. *Scripta Metall* 1972;6:915.
- [26] Donovan PE. *Acta Metall* 1989;37:445.
- [27] Lewandowski JJ, Lowhaphandu P. *Philos Mag A* 2002;82:3427.
- [28] Taub AI. *Acta Metall* 1980;28:633.
- [29] Argon AS, Kuo HY. *Mater Sci Eng* 1979;39:101.
- [30] Argon AS. *Acta Metall* 1979;27:47.
- [31] Argon AS, Shi LT. *Acta Metall* 1983;31:499.
- [32] Srolovitz D, Vitek V, Egami T. *Acta Metall* 1983;31:335.
- [33] Donati C, Douglas JF, Kob W, Plimpton SJ, Poole PH, Glotzer SC. *Phys Rev Lett* 1998;80:2338.
- [34] Gebremichael Y, Vogel M, Glotzer SC. *J Chem Phys* 2004;120:4415.
- [35] Teichler H. *J Non-Cryst Solid* 2002;312–314:533.
- [36] Marcus AH, Schofield J, Rice SA. *Phys Rev E* 1999;60:5725.
- [37] Weeks ER, Weitz DA. *Phys Rev Lett* 2002;89:095704.
- [38] Bains AS, Gordon CA, Granato AV, Schwarz RB. *J Alloys Comp* 2000;310:20.
- [39] Granato AV. *Phys Rev Lett* 1992;68:974.
- [40] Suzuki Y, Haimovich J, Egami T. *Phys Rev B* 1987;35:2162.
- [41] Kuz'minshchev VA, Khonik VA, Dzyuba GA. *Metallofizika* 1991;13:100.
- [42] Swadener G. *Unpublished Results*, Los Alamos National Laboratory; 2004.
- [43] de Hey P, Sietsma J, van den Beukel A. *Acta Mater* 1998;46:5873.
- [44] Tanner R. *Engineering rheology*. Oxford: Clarendon Press; 1988. [chapter 3].
- [45] White JM, Muller SJ. *J Rheol* 2003;47:1467.